

# S4-Driver: Scalable Self-Supervised Driving Multimodal Large Language Model with Spatio-Temporal Visual Representation

Yichen Xie<sup>1,†,\*</sup> Runsheng Xu<sup>2,\*</sup> Tong He<sup>2</sup> Jyh-Jing Hwang<sup>2</sup> Katie Luo<sup>3,†</sup>  
 Jingwei Ji<sup>2</sup> Hubert Lin<sup>2</sup> Letian Chen<sup>4,†</sup> Yiren Lu<sup>2</sup> Zhaoqi Leng<sup>2</sup>  
 Dragomir Anguelov<sup>2</sup> Mingxing Tan<sup>2</sup>

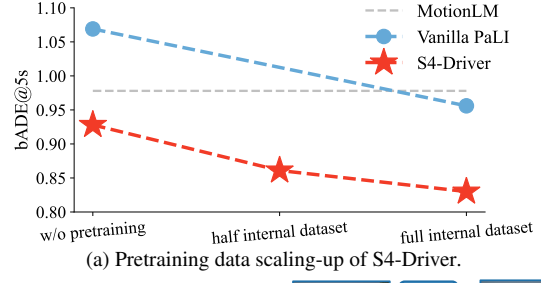
<sup>1</sup> UC Berkeley, <sup>2</sup> Waymo LLC, <sup>3</sup> Cornell University, <sup>4</sup> Georgia Institute of Technology

## Abstract

The latest advancements in multi-modal large language models (MLLMs) have spurred a strong renewed interest in end-to-end motion planning approaches for autonomous driving. Many end-to-end approaches rely on human annotations to learn intermediate perception and prediction tasks, while purely self-supervised approaches—which directly learn from sensor inputs to generate planning trajectories without human annotations—often underperform the state of the art. We observe a key gap in the input representation space: end-to-end approaches built on MLLMs are often pretrained with reasoning tasks in 2D image space rather than the native 3D space in which autonomous vehicles plan. To this end, we propose S4-Driver, a scalable self-supervised motion planning algorithm with spatio-temporal visual representation, based on the popular PaLI [9] multimodal large language model. S4-Driver uses a novel sparse volume strategy to seamlessly transform the strong visual representation of MLLMs from perspective view to 3D space without the need to finetune the vision encoder. This representation aggregates multi-view and multi-frame visual inputs and enables better prediction of planning trajectories in 3D space. To validate our method, we run experiments on both nuScenes and Waymo Open Motion Dataset (with in-house camera data). Results show that S4-Driver performs favorably against existing supervised multi-task approaches while requiring no human annotations. It also demonstrates great scalability when pretrained on large volumes of unannotated driving logs.

## 1. Introduction

The exploration of end-to-end autonomous driving dates back to the 1980s [43], where the motion planning model



(a) Pretraining data scaling-up of S4-Driver.



(b) Multi-task learning framework.



(c) Self-supervised framework.

Figure 1. S4-Driver scaling up with abundant unlabeled driving logs (1a). Different from past efforts that improve MLLM planning via multi-task learning and CoT reasoning (1b), S4-Driver focuses on self-supervised motion planning (1c) without human annotations. While a vanilla PaLI approach with self-supervised training achieves good performance, the full S4-Driver with spatio-temporal visual representation achieves the best performance and scalability (1a).

directly predicts control signals or future waypoints based on raw sensor inputs. Due to limited robustness, these early attempts struggle in complex urban situations. Recent neural network capability advances have led to renewed interest in this field [25, 28, 57], especially given the strong generalization ability of Multimodal Large Language Models (MLLMs) [10, 42, 51].

However, vanilla application of MLLMs to end-to-end motion planning can hardly exploit their strong visual understanding and reasoning capabilities given the significant difference between motion planning and MLLM pretraining tasks, resulting in inferior planning performance [53, 61]. To narrow this gap, as shown in Fig. 1b, previous methods resort to either *multi-task learning*, which incorporates diverse perception and prediction tasks into training and inference, or *supervised perception pretraining*, which utilizes the pretrained autonomous driving perception models as visual tokenizers. However, fine-grained human annotations

<sup>†</sup> Work done when they were interns at Waymo

\* Equal contribution

serve as the bottleneck for both strategies. In contrast, pure self-supervised approaches, while capable of learning directly from sensor inputs and utilizing the abundant unlabeled driving logs, often under-perform the state of the art.

To challenge this status-quo, we aim to boost the performance of self-supervised motion planning orthogonal to prior work (Fig. 1c). It only requires raw sensor data and ego-vehicle trajectories for self-supervised model training, without the need of expensive human labels. First of all, we identify the following two main obstacles in this direction:

- **Suboptimal representation format.** MLLMs [9, 10] are typically designed for tasks in the 2D image plane. This image space representation limits their 3D reasoning ability from the combination of multi-view images.
- **Limited data scale.** Although it is one of the most widely adopted benchmarks for end-to-end planning, nuScenes [5] only contains fewer than 1k sequences and lacks driving behavior diversities. This limited scales leads to severe over-fitting issues in the finetuning of MLLMs with billion-parameter size.

In this paper, we handle the above challenges to better explore the potential of MLLMs. Firstly, we propose **S4-Driver**, a simple yet effective Scalable Self-Supervised motion planning method with Spatio-temporal visual representation. Built upon a general multimodal large language model [9, 10], we directly predict ego-vehicle waypoints from camera images, eliminating the need for intermediate perception and prediction tasks, and thus facilitating the scale-up of model pretraining leveraging massive unannotated driving logs (Fig. 1a). To address the obstacle of suboptimal visual format, we propose a novel sparse volume representation that enables aggregating visual information from multi-view and multi-frame images. Moreover, this spatio-temporal representation is designed to work with frozen features from the perspective-view vision encoder. It boosts 3D spatio-temporal reasoning capabilities of the model on motion planning, and seamlessly preserves world knowledge in the pretrained visual embeddings of MLLMs. Secondly, to rigorously evaluate our method with sufficient training data, we also utilize large-scale WOMD-Planning-ADE benchmark [18] with in-house camera sensor data besides the popular nuScenes dataset [5]. WOMD-Planning-ADE is approximately 100 $\times$  larger than nuScenes, so it serves as a more comprehensive benchmark to evaluate model performance in a scalable manner.

In summary, our contributions include:

- We advocate for a simple self-supervised end-to-end motion planning with MLLMs, solely relying on ego-vehicle trajectory supervision. This approach simplifies the system architecture and facilitates data scaling for training.
- We propose a novel sparse volume representation to effectively aggregate multi-view and multi-frame visual information, enhancing the 3D spatio-temporal reasoning

capabilities of the MLLM for motion planning.

- Our algorithm achieves state-of-the-art performance on both nuScenes and WOMD-Planning-ADE benchmarks. It also demonstrate great scalability with pretraining.

## 2. Related Works

**Multimodal Large Language Models (MLLMs).** MLLMs with both language and images modalities have garnered significant attention in recent years [1, 2, 30, 45, 51]. Prior research has focused on integrating powerful Large Language Models (LLMs) [12, 64, 64] with advanced image encoders [19, 45, 63] such as LLaVA [34], PaLI [9, 10], PaliGemma [4], and InstructBLIP [14]. Through instruction tuning or multi-modal finetuning, these models demonstrate impressive performance in multimodal understanding and reasoning. Current developments are leveraging increasingly larger multimodal datasets to further enhance their capabilities in complex perception and generalization tasks [3, 42, 59]. However, despite their strengths, these models have shown limitations in 3D spatial reasoning [11, 22, 40], posing challenges for their application in autonomous driving.

**End-to-end Autonomous Driving.** While the key final step of autonomous driving is planning, traditional systems are often assembled with multiple modules for perception [33, 35, 60] and prediction [41, 54, 65] tasks. To mitigate the information loss and error accumulation across modules, end-to-end driving systems [6, 24, 25, 28, 32, 66] utilize a unified model to predict the ego-vehicle future waypoints or control signals directly from raw sensor inputs. While prioritizing planning, these systems typically still incorporate perception and prediction, requiring explicit supervision for each. Although some prior works [13, 46, 58] have explored pure motion planning without any intermediate tasks, they struggle in complex urban scenarios due to modeling capability limitations.

**MLLMs for Driving.** The superior reasoning and generalization abilities of large-scale models are desirable properties for autonomous driving. Some efforts transform the driving scenario into large language model textual prompts [8, 38, 47] or directly process camera images with vision-language models [15, 48, 61]. However, their potential is limited to the small scale of existing benchmarks [5], which only allow partial finetuning [23]. Meanwhile, closed-loop simulators [16] struggle to provide realistic sensor data for end-to-end tasks. Consequently, multi-task joint finetuning [49, 53, 61] or chain-of-thought (CoT) [56] inference [37–39] are widely adopted to simplify the reasoning despite the extra annotation requirements brought by perception and prediction modules. Alternatively, some work [15, 52] integrates pretrained perception models [31] to extract BEV features and sends to

language models as vision tokens. Recently, EMMA [26] leverages powerful Gemini [51] for self-supervised motion planning. Additionally, they develop a mixture of training tasks, including motion planning, 3D object detection, and road graph estimation as well as additional reasoning process for trajectory generation. In contrast, our work focuses on the enhancement of self-supervised motion planning without extra human labels.

### 3. Enhancing MLLM for Motion Planning

In this section, we adapt a pretrained MLLM for the end-to-end motion planning task. Without loss of generality, we leverage PaLI [10]. However, these techniques are also compatible with other more powerful MLLMs. We introduce a set of design improvements to the MLLM setup and demonstrate correspondingly improved performance on WOMD-Planning-ADE (Fig. 3).

#### 3.1. Vanilla PaLI as Planner

End-to-end motion planning models determine the future trajectory  $\mathcal{O}_{T_f}$  of ego-vehicle based on multi-view camera images  $\mathcal{C}$  and high-level behavior command  $b$ . The future trajectory consists of the ego-vehicle’s location at each future time step in the BEV coordinate, *i.e.*  $\mathcal{O}_{T_f} = [(x_t, y_t)]_{t=1}^{T_f}$ . The high-level behavior command is necessary to guide the driving direction, similar to a navigation system. Additionally, as verified in prior works [32, 62], the historical states of ego-vehicle  $\mathcal{H}_{T_h}$  are also critical for a smooth and feasible planning result, where we consider the historical locations, velocities, and accelerations as  $\mathcal{H}_{T_h} = [\mathbf{l}_t, \mathbf{v}_t, \mathbf{a}_t]_{t=-1}^{-T_h}$ , *i.e.*

$$\mathcal{O}_{T_f} = P(\mathcal{C}, \mathcal{H}_{T_h}, b) \quad (1)$$

where  $P(\cdot)$  is the planning model. We provide both historical ego states and high-level commands to the model as text prompts. Locations, velocities, and accelerations are represented directly as floating numbers with two decimals. The predicted future trajectories are then extracted from the decoded text outputs of the model. Example prompts and targets are provided in the supplementary materials.

Without preceding perception and prediction tasks, the vanilla PaLI, fine-tuned in a self-supervised manner, achieves reasonable but not ideal performance in motion planning (Fig. 3).

#### 3.2. Hierarchical Planning with Meta-Decision

Directly outputting a future trajectory without any reasoning is challenging for MLLMs. To address this, we apply a coarse-to-fine approach, inspired by Chain-of-Thought (CoT) [56]. It adopts a hierarchical planning method [27], going from semantic decision to numeric planning. We prompt our model to provide a high-level estimation of

the future acceleration state  $D$  first, effectively decomposing the motion planning task into two steps:

$$D = P_{s1}(\mathcal{C}, \mathcal{H}_{T_h}, b), \quad \mathcal{O}_{T_f} = P_{s2}(\mathcal{C}, \mathcal{H}_{T_h}, b; D) \quad (2)$$

We define  $D$  to encompass four meta-decisions: *keep stationary*, *keep speed*, *accelerate* and *decelerate*. Notably, unlike previous CoT applications in VLM-based planning that require human annotation for training, such as the scene analysis in DriveVLM [53], we incorporate these meta-decisions as a “free lunch” to simplify the motion planning process without requiring any additional annotations. The ground-truth decisions are generated by heuristic rules based on the future ego velocity and acceleration (details in the supplementary materials). Fig. 3 shows this simple design brings non-trivial improvements in planning performance.

#### 3.3. Scene Representation in 3D Space

High-quality motion planning requires a robust understanding of the surrounding 3D scene, including both static and dynamic elements. While traditionally achieved through separate perception and prediction modules, our self-supervised end-to-end framework relies on the MLLM to implicitly learn this understanding without explicit supervision. However, despite strong 2D reasoning capabilities, MLLMs often struggle with 3D spatial reasoning due to limitations in their perspective view representation and the lack of depth-related tasks in pretraining [7, 36].

##### 3.3.1. 3D Visual Representation with Dense Volumes

To overcome the above limitations, we draw inspiration from previous successful perception tasks [31, 35] and adopt a 3D volume representation. The multi-view feature maps  $\mathcal{F}_{2D} = \{\mathbf{f}_{2D}^v\}_{v=1}^V$  ( $\mathbf{f}_{2D}^v \in \mathbb{R}^{H \times W \times C}$ ) are extracted by visual encoder of MLLM, where  $V$  is the number of views. We construct a 3D feature volume  $\mathbf{f}_{3D}^{vol} \in \mathbb{R}^{X \times Y \times Z \times C}$  centered at the ego-vehicle based on the multi-view image features. To avoid introducing complex modules that might disrupt the pretrained MLLM and misalign visual features with the subsequent multimodal encoder-decoder, we employ a lightweight projection method, similar to Simple-BEV [20]. Specifically, for each voxel in the 3D volume, we project its  $(x, y, z)$  coordinates to each perspective view  $v$ , obtaining corresponding 2D coordinates  $(u_v, v_v)$ . We then bilinearly sample the local features from each view at these projected locations. Finally, the voxel’s feature representation is computed as the average of the local semantic features from all views where the voxel projects within the image bounds. This process effectively incorporates 3D spatial information while maintaining compatibility with the pretrained MLLM.

$$\mathbf{f}_{3D, (x, y, z)}^{vol} = \mathbf{f}_{(x, y, z)}^{sem} + \text{PosEmb}(x, y, z) \quad (3)$$

$$\mathbf{f}_{(x, y, z)}^{sem} = \text{Avg}(\{\text{Bilinear}(\mathbf{f}_{2D}^v; (u_v, v_v))\}_v) \quad (4)$$

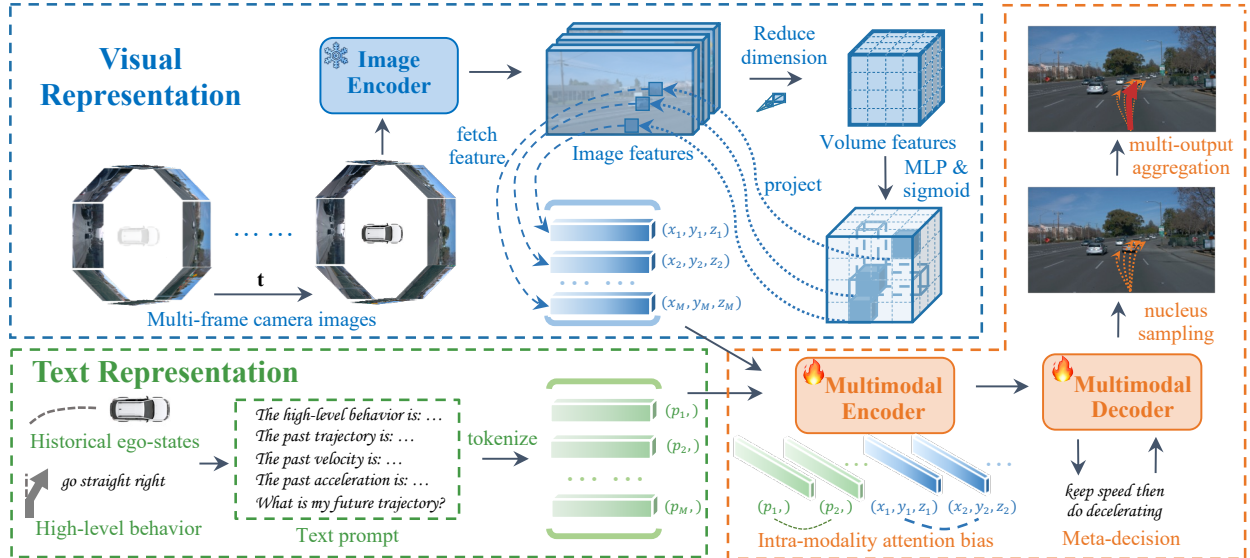


Figure 2. Overview of our proposed S4-Driver algorithm. We enhance the PaLI model for motion planning by incorporating meta-decision, spatio-temporal visual representation, and multi-decoding aggregation.

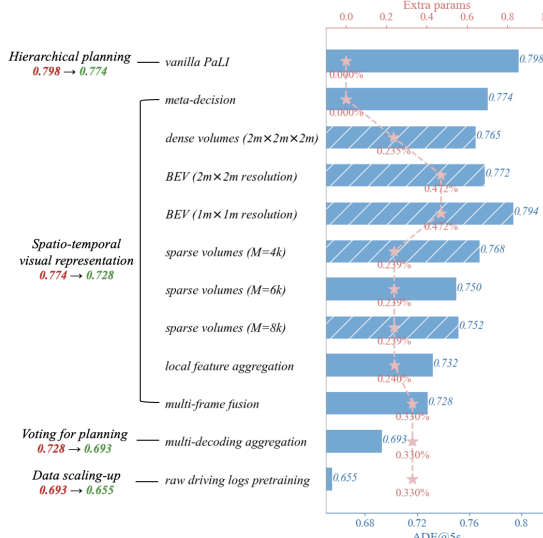


Figure 3. A roadmap for enhancing MLLM for planning. The techniques are adopted step-by-step from top to bottom, while shadow items are not adopted in the subsequent steps. We show the performance on WOMD-Planning-ADE (Sec. 4) after including each module.

This simple and efficient projection strategy ensures that the 3D volume features  $\mathbf{f}_{3D}^{vol}$  share a similar distribution with the original multi-view features  $\mathcal{F}_{2D}$ . This similarity facilitates seamless integration with the subsequent multimodal encoder-decoder of the MLLM.

As shown in Fig. 3, this 3D volume representation leads to some improvement in motion planning performance. Alternatively, we find that reducing the  $Z$ -axis using a fully connected layer to obtain a BEV representation yields slightly worse performance since this reduction operation

may introduce ambiguity to the scene representation.

### 3.3.2. Sparse Volume Representation

While the 3D volume representation effectively captures spatial information, inherently most of the surrounding 3D space is empty. Moreover, for motion planning, detailed information about objects distant from the road, such as buildings and trees, is less critical. Based on this observation, we propose a sparse volume representation to reduce the number of voxels, enabling higher resolution given memory constraints and improving efficiency.

To determine useful volumes in each scene based on their positions and semantics, we define a gate value  $g_{(x,y,z)}^{vol} \in (0, 1)$  for each volume at coordinates  $(x, y, z)$ . To obtain this gate, starting from multi-view image features  $\{\mathbf{f}_{2D}^v\}_{v=1}^V$ , we reduce its dimension through a fully connect (FC) layer as

$$\mathbf{f}_{2D}^{gate,v} = \text{FC}(\mathbf{f}_{2D}^v), \quad \mathbf{f}_{2D}^{gate,v} \in \mathbb{R}^{H \times W \times C'}, C' \ll C. \quad (5)$$

Then we construct a reduced-dimension volume feature  $\mathbf{f}_{3D}^{gate} \in \mathbb{R}^{X \times Y \times Z \times C'}$  from  $\{\mathbf{f}_{2D}^{gate,v}\}_{v=1}^V$  same as Eq. 3. A smaller channel number allows for larger volume resolution and is sufficient to indicate whether a volume is related to motion planning. Afterward, the gate is derived from  $\mathbf{f}_{3D}^{gate}$  through a small MLP module as follows.

$$g_{(x,y,z)}^{vol} = \text{sigmoid} \left( \text{MLP}(\mathbf{f}_{3D}^{gate,(x,y,z)}) \right) \quad (6)$$

Thus, we can easily select  $M$  volumes ( $M \ll X \cdot Y \cdot Z$ ) with largest gate values with coordinates  $\{(x_i, y_i, z_i)\}_{i=1}^M$ .

As we do not have access to ground-truth occupancy state, we propose learning the gate values implicitly. We

assume that regions with small gate values should be empty or irrelevant to planning. For these vacant space, we assign a learnable feature  $\mathbf{f}_{vac} \in \mathbb{R}^C$ . We expect the model can learn the gate value via the trade-off between the semantic features and this vacant feature at each 3D position, so we fetch features for selected sparse volumes as

$$\mathbf{f}_{3D,(x,y,z)}^{sparse} = \hat{\mathbf{f}}_{3D,(x,y,z)}^{sparse} + \text{PosEmb}(x, y, z) \quad (7)$$

$$\hat{\mathbf{f}}_{3D,(x,y,z)}^{sparse} = g_{(x,y,z)}^{vol} \cdot \mathbf{f}_{(x,y,z)}^{sem} + (1 - g_{(x,y,z)}^{vol}) \cdot \mathbf{f}_{vac} \quad (8)$$

where  $\mathbf{f}_{(x,y,z)}^{sem}$  is same as Eq. 4 and  $(x, y, z) \in \{(x_i, y_i, z_i)\}_{i=1}^M$  are selected volumes with large gate values. When the sparse volume features  $\mathbf{f}_{3D,(x,y,z)}^{sparse}$  are fed into the subsequent multimodal encoder, they notably boost the planning performance (Fig. 3) by simultaneously providing explicit 3D spatial cues of surrounding scenes and concentrate on the important regions adaptively.

### 3.3.3. Local Feature Aggregation in 3D Space

Due to the lack of depth information, the lifting process in Eq. 3 or 7 results in duplicate volume features along each camera ray. This spatial ambiguity can be mitigated by 3D local operations like convolutions [20] or deformable attention [31] as demonstrated in previous work. However, in our MLLM framework, it is less economical to insert extra local operations. Instead, we inject some relative position bias into the existing multimodal encoder by tailoring the self-attention as follows.

$$\text{Attn}(Q, K, V) = \text{Softmax} \left( \frac{QK^T}{\sqrt{d}} - b(D) \right) V \quad (9)$$

Given  $M$  sparse volumes with coordinates  $\{(x_i, y_i, z_i)\}_{i=1}^M$ , the distance matrix  $D \in \mathbb{R}^{M \times M \times 3}$  is the distance along  $xyz$ -axes between each pair of sparse volumes, *i.e.*  $D_{ij} = (x_j - x_i, y_j - y_i, z_j - z_i)$ . The bias is computed with the function  $b(\Delta x, \Delta y, \Delta z) = b_x(\Delta x) + b_y(\Delta y) + b_z(\Delta z)$ , where  $\Delta x, \Delta y, \Delta z$  are divided into several bins and mapped to a learnable bias value for each bin through  $b_x(\cdot), b_y(\cdot), b_z(\cdot)$ . We also apply a separate bias between the text tokens with 1D position  $\{p_i\}$ .

This relative position bias elegantly inserts local inductive bias to pretrained global self-attention modules with minimal additional costs. It leads to a notable performance gain in Fig. 3 by facilitating the aggregation of local information in 3D space, enhancing scene understanding and spatial reasoning.

### 3.4. Multi-frame Temporal Fusion

Multi-frame input combination helps to compensate for the lack of depth cues in camera images. We extend our sparse volume representation to aggregate multi-frame temporal information by incorporating  $T$  historical frames with an interval of  $0.5s$ . Given images from the total  $T + 1$  frames,

Eq. 5 is applied to each frame separately to obtain the multi-view image features  $\mathbf{f}_{2D,t,v}^{gate,v}, t = 0, -1, \dots, -T, v = 1, \dots, V$ . After ego-motion compensation, we construct a gate feature volume  $\mathbf{f}_{3D,t}^{gate}$  based on the current ego-vehicle coordinates and per-frame image features. Multi-frame volume features are concatenated along the channel dimension to generate gate value.

$$g_{(x,y,z)}^{vol} = \text{sigmoid} \left( \text{MLP} \left( \text{Concat} \left( [\mathbf{f}_{3D,t,(x,y,z)}^{gate}]_{t=0}^{-T} \right) \right) \right) \quad (10)$$

Similar with Sec. 3.3.2, we select  $M$  volumes based on the gate value. Following Eq. 7, the volume features are fetched from each frame image feature map separately as  $\mathbf{f}_{3D,t,(x,y,z)}^{sparse}, t = 0, \dots, -T$ , which are fused with an FC-layer as the sparse volume feature with temporal awareness.

$$\mathbf{f}_{3D,(x,y,z)}^{sparse} = \text{FC} \left( \text{Concat} \left( [\mathbf{f}_{3D,t,(x,y,z)}^{sparse}]_{t=0}^{-T} \right) \right) \quad (11)$$

In Fig. 3, temporal fusion helps to improve motion planning performance by facilitating the environment understanding.

### 3.5. Voting for Planning via Multi-Decoding

MLLMs are prone to assigning high confidence to the simple future behaviors in motion planning, *e.g.*, keeping stationary. To relieve this bias, we aggregate multiple outputs and use voting to obtain the final planning output. We resort to nucleus sampling [21] to produce multiple future trajectories for the ego-vehicle, denoted as  $\{\mathcal{O}_{T_f}^k\}_{k=1}^K$ . They are simply averaged to produce a unique planning result as follows:  $\mathcal{O}_{T_f} = [(x_t, y_t)]_{t=1}^{T_f}$ .

$$(x_t, y_t) = \left( \frac{1}{K} \sum_{k=1}^K x_t^k, \frac{1}{K} \sum_{k=1}^K y_t^k \right) \quad (12)$$

This unweighted average mitigates the MLLM's bias towards simple behaviors. Fig. 3 demonstrates the notable performance gain with this simple multi-decoding aggregation approach.

### 3.6. Scaling to Large-scale Raw Driving Logs

The self-supervised training allows our proposed S4-Driver to scale to large-scale driving logs amounts without requiring human annotations. To exploit the potential of MLLM-based planners, we pretrain the model on our internal dataset. Results in Fig. 3 demonstrate that S4-Driver achieves notable performance gains in challenging tail behaviors due to large-scale pretraining.

## 4. Waymo Open Motion Dataset for Planning

For the large-scale training and evaluation of planning algorithms with large models, we design a WOMD-Planning-ADE benchmark based on WOMD dataset [18], and compare with the existing datasets in Tab. 1.

Benchmark	Size		Data Format		Metrics	
	Sequence	Length	Frequency	Planning horizon	Sample-wise	Behavior-wise
BDD-X [29]	7k	77 h	10 Hz	control signal	✓	✗
nuScenes [5]	1k	5.5 h	2 Hz	3s	✓	✗
WOMD-Planning-ADE	103k	574 h	10 Hz	5s	✓	✓

Table 1. Comparisons between WOMD-Planning-ADE and existing counterparts. WOMD-Planning-ADE has a significantly larger size and more comprehensive behavior-wise metrics.

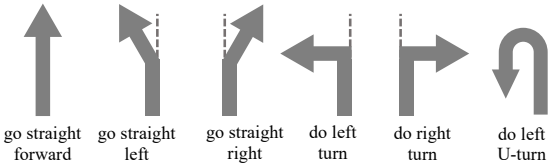


Figure 4. High-level behavior commands for motion planning.

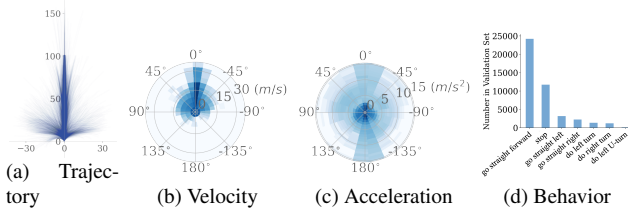


Figure 5. Statistical distributions of WOMD-Planning-ADE. We show the distributions of ego-vehicle trajectories, velocities, accelerations and each behavior scenario sizes in the validation set.

**Overview.** It contains 103k real-world driving scenarios, covering diverse urban and suburban scenes. They are further divided into 9s samples with 1s history and 8s future. For end-to-end planning evaluation, besides the ego-vehicle trajectories in each sample as groundtruth, we also have the following key items in the dataset:

**(In-house) Camera Data.** Most end-to-end planning methods [28, 49, 53, 61] relies on the camera images as model inputs. In our dataset, each frame contains images captured by eight multi-view cameras.

**High-level Behavior Commands.** Like navigation systems for humans (e.g. Google Map), the end-to-end planning system also requires navigation signals to indicate the direction to go. We consider six high-level behavior commands (Fig. 4), namely *go straight forward*, *go straight left*, *go straight right*, *do left turn*, *do right turn*, *do left U-turn*. They can cover diverse driving situations in real world, e.g. “*go straight right*” describes the case to leave the high-way. Instead of simply considering the last step position [6, 25], we decide the behavior commands based on long-term future trajectories, which can handle the low-speed or stopping situations. Details of this heuristic rule are included in the supplementary materials.

**Evaluation Metrics.** The imbalance of data distribution is inevitable in real driving scenarios. For example, in the WOMD-Planning-ADE benchmark, moving straight and stopping account for more than 70% of all the samples, as

reflected by Fig. 5. In this case, we argue that current widely used sample-wise average displacement error and collision rates cannot comprehensively reflect the performance of motion planning algorithms since challenging but less frequent behaviors, like turning, are overwhelmed by simple straightforward moving scenarios. To this end, we propose novel behavior-wise metrics similar to the mAP metric in prediction [18]. For example, we denote the behavior-wise average displacement error as  $bADE$  defined as follows.

$$bADE = \frac{1}{|\mathcal{B}|} \sum_{b \in \mathcal{B}} ADE_b \quad (13)$$

where  $ADE_b$  is the ADE metric for a specific behavior. Concretely,  $|\mathcal{B}| = 7$  behaviors are considered – including the six high-level commands (Fig. 4) and an additional *stop* behavior<sup>1</sup>. These behavior-wise metrics make up for the shortcomings of previous sample-wise metrics by paying more attention to those scarce but safety-critical behaviors.

## 5. Experiments

### 5.1. Implementation Details

**Model and finetuning.** Unless otherwise specified, we construct our model from a pretrained PaLI3-5B model [10], which includes a ViT-G (2B) vision encoder [17] and multimodal encoder-decoder (3B) [50]. Our default setting freezes the ViT encoder and finetune only the inserted modules and the multimodal encoder-decoder. Finetuning the model on the WOMD-Planning-ADE dataset requires approximately 2.5 days on 128 Google Cloud TPU v4 using a batch size of 256 and a learning rate of 3e-3.

**Datasets.** We evaluate S4-Driver on both WOMD-Planning-ADE (Sec. 4) and nuScenes [5] benchmarks. Given the limited size of nuScenes, which is insufficient for training a multimodal large language model, we also attempt to finetune the model on nuScenes using weights pretrained on WOMD-Planning-ADE.

### 5.2. Main Results and Comparison

**NuScenes dataset.** To widely compare with existing end-to-end planning methods in the community, we evaluate S4-Driver on nuScenes dataset [5]. Tab. 2 show that S4-Driver notably outperforms all the previous algorithms despite its self-supervised training format. Unlike existing works, S4-Driver does not require any perception pretraining or human annotations. This self-supervision nature enables S4-Driver to utilize all the accessible raw trajectory data, whereas these easily collectable raw driving logs offer limited benefit to other algorithms without a labeling process.

<sup>1</sup>We do not include “stop” in the high-level behavior commands since navigation system cannot provide it and this may leak future information like traffic lights. Details are explained in supplementary materials.

Methods	Human Annotations		Extra Data		$L_2(m)$			
	perception	prediction	data	labels	1.0s	2.0s	3.0s	$Avg_{1,2,3s}$
<i>Multi-task end-to-end approaches</i>								
UniAD [25]	✓	✓	✗	✗	0.42	0.64	0.91	0.66
VAD [28]	✓	✓	✗	✗	0.17	0.34	0.60	0.37
PARA-Drive [57]	✓	✓	✗	✗	0.25	0.46	0.74	0.48
<i>Multimodal large language model approaches</i>								
GPT-Driver [38]	✓	✓	✗	✗	0.20	0.40	0.70	0.44
DriveVLM [53]	✓	✓	✓	✓	0.18	0.34	0.68	0.40
OmniDrive [55]	✓	✓	✓	✓	0.14	0.29	0.55	0.33
<i>Self-supervised approaches</i>								
DriveVLM (w/o CoT) [53]	✗	✗	✓	✗	0.19	0.41	0.89	0.49
S4-Driver (ours)	✗	✗	✗	✗	0.16	0.34	0.63	0.38
S4-Driver* (ours)	✗	✗	✓	✗	<b>0.13</b>	<b>0.28</b>	<b>0.51</b>	<b>0.31</b>

Table 2. NuScenes benchmark results. Most previous works require human annotations as additional supervision. S4-Driver\* is pretrained on WOMD-Planning-ADE, while many prior MLLM-based methods also utilize extra data and labels due to the limited scale of nuScenes.

Methods	Sample-wise Metrics			Behavior-wise Metrics		
	ADE@1s	ADE@3s	ADE@5s	bADE@1s	bADE@3s	bADE@5s
Vanilla PaLI	0.034	0.277	0.798	0.051	0.392	1.069
S4-Driver (ours)	0.031	0.247	0.693	0.049	0.350	0.928
S4-Driver* (ours)	<b>0.029</b>	<b>0.233</b>	<b>0.655</b>	<b>0.044</b>	<b>0.313</b>	<b>0.830</b>
<i>Models that utilize high-quality objects, tracks, and roadgraph as inputs rather than raw camera images.</i>						
MotionLM [46]	0.045	0.266	0.697	0.066	0.388	0.978

Table 3. WOMD-Planning-ADE benchmark results. “\*” denotes methods pretrained on the internal dataset.

**WOMD-Planning-ADE benchmark.** In Tab. 3, we primarily compare S4-Driver with the vanilla PaLI3-5B baseline (Sec. 3.1) and modular algorithm MotionLM [46]. Compared with vanilla PaLI3-5B, a notable gap is witnessed for both sample-wise and behavior-wise metrics. For reference, we also adapt a latest motion prediction algorithms MotionLM [46] (enhanced internally reproduced version) for planning task by only predicting the future trajectories of ego-vehicle and injecting the high-level command to the model. Because it utilizes auto-labelled high-quality objects, tracklets, and roadgraph signals as model inputs [44], a direct comparison with our end-to-end approaches is not equitable. However, as shown in Tab. 3, S4-Driver still achieves favorable performance compared to MotionLM, particularly in behavior-wise metrics even if S4-Driver uses only raw camera images as inputs.

### 5.3. Analysis

**Qualitative results.** Fig. 6 visualizes planning results in diverse scenarios. Our proposed S4-Driver can determine the future ego-behavior based on the traffic lights and road lane. It can also complete challenging behaviors and deal

with different lighting conditions. We will include more visualizations in supplementary materials.

**Meta-decision reliability.** Fig. 7 demonstrates the accuracy of meta-decision prediction (Sec. 3.2) on WOMD-Planning-ADE validation set. Across all behaviors, the model provides reliable meta-decision estimations. Without any human annotations, this preliminary prediction can simplify the derivation of numeric motion planning.

**Distribution of sparse volumes.** We visualize the distribution of self-supervised learned sparse volumes along x-axis and y-axis over WOMD-Planning-ADE validation set in Fig. 8. From back to front, the sparse volumes concentrate on the close front region. From left to right, the sparse volumes cover all the regions, since there are turning scenarios, but most volumes focus on the middle region. These distributions are consistent with human driving experiences.

### 5.4. Ablation Studies

This section presents experiments conducted on the WOMD planning benchmark to clarify the roles of specific modules within our S4-Driver algorithm. More ablation studies are available in the supplementary material.

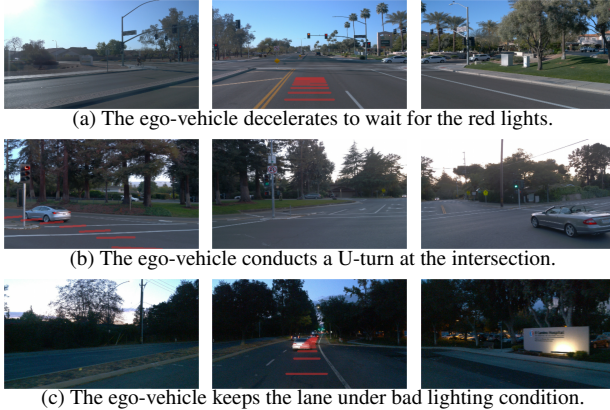


Figure 6. Qualitative results of motion planning. We show the *front left*, *front*, *front right* cameras for each case.

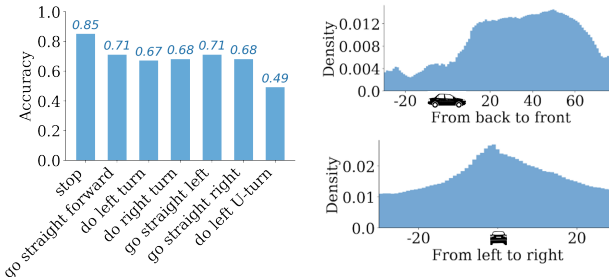


Figure 7. Meta-decision prediction accuracy for each behavior.

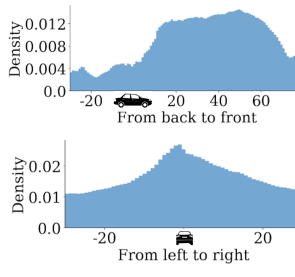


Figure 8. Distribution of sparse volumes along x- and y-axes.

**MLLM inputs.** In Tab. 5, we analyze the roles of camera images and historical ego-states separately using the vanilla PaLI model. Consistent with [32, 62], the importance of ego-states is acknowledged. Meanwhile, different from their observations on nuScenes benchmark, camera inputs also make great differences on WOMD-Planning-ADE. We assume that WOMD-Planning-ADE covers more diverse driving scenarios including many severe changes of speed and directions, which attaches importance to the sensor data. This also showcases the advantages of WOMD-Planning-ADE for comprehensive evaluation. Tab. 5 also shows that random initialized model cannot converge without MLLM pretraining. Despite different domains, S4-Driver can profit from the strong reasoning ability from large-scale MLLM pretraining on general tasks.

**MLLM capability.** In addition to the PaLI3-5B [10] used in other parts, we also tailor PaLI2-3B [9] for motion planning with the same techniques. PaLI2-3B is weaker in parameter numbers (3B vs. 5B), architecture, pretraining manner, and input resolution (224 vs. 448). As in Tab. 4, S4-Driver based on PaLI2-3B demonstrates much inferior performance compared to that based on PaLI3-5B. We conduct experiments on two different training data scales on WOMD-Planning-ADE, *i.e.* 20k (nuScenes scale) vs. 400k (full WOMD-Planning-ADE). The gap is particularly large given enough training data. It also justifies the necessity to

MLLM	WOMD-Planning-ADE Subset (20k)		Full WOMD-Planning-ADE (400k)	
	ADE@5s	bADE@5s	ADE@5s	bADE@5s
PaLI2-3B [9]	1.241	1.846	1.035	1.522
PaLI3-5B [10]	<b>1.075</b>	<b>1.495</b>	<b>0.693</b>	<b>0.928</b>

Table 4. Ablation studies on planning performance scalability of our methods w.r.t. model and data sizes. We experiment with two MLLMs on two different training data sizes.

Method	ADE@5s	bADE@5s
vanilla PaLI	<b>0.798</b>	<b>1.069</b>
w/o historical states	2.009	2.250
w/o camera images	1.081	1.448
w/o MLLM pretraining	fail to converge	

Table 5. Ablation studies on MLLM inputs.

Resolution	ADE@5s	bADE@5s
2m × 2m × 2m	0.798	1.201
1m × 1m × 2m	<b>0.750</b>	<b>1.005</b>
1m × 1m × 1m	0.765	1.051

Table 6. Ablation studies on sparse volume resolutions.

conduct experiments on large-scale dataset, which can fully unleash the potential of powerful MLLMs.

**Sparse volume resolution.** Tab. 6 shows the results with different resolution for sparse volumes with same number of sparse volumes ( $M = 6000$ ). In line with Fig. 3, low resolution leads to relatively worse performance since it limits the precision of 3D spatial reasoning. Interestingly, higher resolution along  $z$ -axis does not definitely improve the model performance since the motion planning mainly works on the  $xy$ -plane and too low sparsity ratio tends to make the optimization unstable.

## 6. Conclusion and Future Work

This paper introduces S4-Driver, a scalable self-supervised motion planning framework for autonomous driving that utilizes Multimodal Large Language Models (MLLMs). To enhance 3D reasoning in MLLMs, we propose a novel sparse volume representation, which enables improved spatio-temporal reasoning through the aggregation of multi-view and multi-frame image inputs. Additionally, we design behavior-wise metrics for comprehensive evaluation on the large-scale WOMD-Planning-ADE benchmark. S4-Driver achieves state-of-the-art performance on both nuScenes and WOMD-Planning-ADE benchmarks, without requiring any human annotations. This demonstrates the potential of self-supervised learning for end-to-end autonomous driving. Future work will involve applying our methods to other powerful MLLM architectures. Our contributions are orthogonal to previous works, such as those that explore multi-task learning or CoT reasoning [49, 55]. Combining our large-scale self-supervised

learning approach with supervised finetuning on targeted small-scale labeled data may further enhance the final performance and interpretability of the system.

## References

[1] Josh Achiam, Steven Adler, Sandhini Agarwal, Lama Ahmad, Ilge Akkaya, Florencia Leoni Aleman, Diogo Almeida, Janko Altenschmidt, Sam Altman, Shyamal Anadkat, et al. Gpt-4 technical report. *arXiv preprint arXiv:2303.08774*, 2023. [2](#)

[2] Jean-Baptiste Alayrac, Jeff Donahue, Pauline Luc, Antoine Miech, Iain Barr, Yana Hasson, Karel Lenc, Arthur Mensch, Katherine Millican, Malcolm Reynolds, et al. Flamingo: a visual language model for few-shot learning. *Advances in neural information processing systems*, 35:23716–23736, 2022. [2](#)

[3] Jinze Bai, Shuai Bai, Shusheng Yang, Shijie Wang, Sinan Tan, Peng Wang, Junyang Lin, Chang Zhou, and Jingren Zhou. Qwen-vl: A versatile vision-language model for understanding, localization, text reading, and beyond. *arXiv preprint arXiv:2308.12966*, 1(2):3, 2023. [2](#)

[4] Lucas Beyer, Andreas Steiner, André Susano Pinto, Alexander Kolesnikov, Xiao Wang, Daniel Salz, Maxim Neumann, Ibrahim Alabdulmohsin, Michael Tschanen, Emanuele Bugliarello, et al. Paligemma: A versatile 3b vlm for transfer. *arXiv preprint arXiv:2407.07726*, 2024. [2](#)

[5] Holger Caesar, Varun Bankiti, Alex H Lang, Sourabh Vora, Venice Erin Liong, Qiang Xu, Anush Krishnan, Yu Pan, Giacarlo Baldan, and Oscar Beijbom. nuscenes: A multi-modal dataset for autonomous driving. In *Proceedings of the IEEE/CVF conference on computer vision and pattern recognition*, pages 11621–11631, 2020. [2, 6](#)

[6] Sergio Casas, Abbas Sadat, and Raquel Urtasun. Mp3: A unified model to map, perceive, predict and plan. In *Proceedings of the IEEE/CVF Conference on Computer Vision and Pattern Recognition*, pages 14403–14412, 2021. [2, 6](#)

[7] Boyuan Chen, Zhuo Xu, Sean Kirmani, Brain Ichter, Dorsa Sadigh, Leonidas Guibas, and Fei Xia. Spatialvilm: Endowing vision-language models with spatial reasoning capabilities. In *Proceedings of the IEEE/CVF Conference on Computer Vision and Pattern Recognition*, pages 14455–14465, 2024. [3](#)

[8] Long Chen, Oleg Sinavski, Jan Hünermann, Alice Karnsund, Andrew James Willmott, Danny Birch, Daniel Maund, and Jamie Shotton. Driving with llms: Fusing object-level vector modality for explainable autonomous driving. In *2024 IEEE International Conference on Robotics and Automation (ICRA)*, pages 14093–14100. IEEE, 2024. [2](#)

[9] Xi Chen, Xiao Wang, Soravit Changpinyo, AJ Piergiovanni, Piotr Padlewski, Daniel Salz, Sebastian Goodman, Adam Grycner, Basil Mustafa, Lucas Beyer, et al. Pali: A jointly-scaled multilingual language-image model. In *The Eleventh International Conference on Learning Representations*. [1, 2, 8](#)

[10] Xi Chen, Xiao Wang, Lucas Beyer, Alexander Kolesnikov, Jialin Wu, Paul Voigtlaender, Basil Mustafa, Sebastian Goodman, Ibrahim Alabdulmohsin, Piotr Padlewski, et al. Pali-3 vision language models: Smaller, faster, stronger. *arXiv preprint arXiv:2310.09199*, 2023. [1, 2, 3, 6, 8](#)

[11] An-Chieh Cheng, Hongxu Yin, Yang Fu, Qiushan Guo, Ruihan Yang, Jan Kautz, Xiaolong Wang, and Sifei Liu. Spatialrgpt: Grounded spatial reasoning in vision language model. *arXiv preprint arXiv:2406.01584*, 2024. [2](#)

[12] Hyung Won Chung, Le Hou, Shayne Longpre, Barret Zoph, Yi Tay, William Fedus, Yunxuan Li, Xuezhi Wang, Mostafa Dehghani, Siddhartha Brahma, et al. Scaling instruction-finetuned language models. *Journal of Machine Learning Research*, 25(70):1–53, 2024. [2](#)

[13] Felipe Codevilla, Matthias Müller, Antonio López, Vladlen Koltun, and Alexey Dosovitskiy. End-to-end driving via conditional imitation learning. In *2018 IEEE international conference on robotics and automation (ICRA)*, pages 4693–4700. IEEE, 2018. [2](#)

[14] Wenliang Dai, Junnan Li, Dongxu Li, Anthony Meng Huat Tiong, Junqi Zhao, Weisheng Wang, Boyang Li, Pascale Fung, and Steven Hoi. Instructblip: Towards general-purpose vision-language models with instruction tuning, 2023. [2](#)

[15] Xinpeng Ding, Jianhua Han, Hang Xu, Xiaodan Liang, Wei Zhang, and Xiaomeng Li. Holistic autonomous driving understanding by bird’s-eye-view injected multi-modal large models. In *Proceedings of the IEEE/CVF Conference on Computer Vision and Pattern Recognition*, pages 13668–13677, 2024. [2](#)

[16] Alexey Dosovitskiy, German Ros, Felipe Codevilla, Antonio Lopez, and Vladlen Koltun. Carla: An open urban driving simulator. In *Conference on robot learning*, pages 1–16. PMLR, 2017. [2](#)

[17] Alexey Dosovitskiy, Lucas Beyer, Alexander Kolesnikov, Dirk Weissenborn, Xiaohua Zhai, Thomas Unterthiner, Mostafa Dehghani, Matthias Minderer, Georg Heigold, Sylvain Gelly, et al. An image is worth 16x16 words: Transformers for image recognition at scale. *arXiv preprint arXiv:2010.11929*, 2020. [6](#)

[18] Scott Ettinger, Shuyang Cheng, Benjamin Caine, Chenxi Liu, Hang Zhao, Sabeek Pradhan, Yuning Chai, Ben Sapp, Charles R Qi, Yin Zhou, et al. Large scale interactive motion forecasting for autonomous driving: The waymo open motion dataset. In *Proceedings of the IEEE/CVF International Conference on Computer Vision*, pages 9710–9719, 2021. [2, 5, 6](#)

[19] Yuxin Fang, Wen Wang, Binhui Xie, Quan Sun, Ledell Wu, Xinggang Wang, Tiejun Huang, Xinlong Wang, and Yue Cao. Eva: Exploring the limits of masked visual representation learning at scale. In *Proceedings of the IEEE/CVF Conference on Computer Vision and Pattern Recognition*, pages 19358–19369, 2023. [2](#)

[20] Adam W Harley, Zhao yuan Fang, Jie Li, Rares Ambrus, and Katerina Fragkiadaki. Simple-bev: What really matters for multi-sensor bev perception? In *2023 IEEE International Conference on Robotics and Automation (ICRA)*, pages 2759–2765. IEEE, 2023. [3, 5](#)

[21] Ari Holtzman, Jan Buys, Li Du, Maxwell Forbes, and Yejin Choi. The curious case of neural text degeneration. *arXiv preprint arXiv:1904.09751*, 2019. [5, 1](#)

[22] Yining Hong, Haoyu Zhen, Peihao Chen, Shuhong Zheng, Yilun Du, Zhenfang Chen, and Chuang Gan. 3d-llm: Injecting the 3d world into large language models. *Advances in Neural Information Processing Systems*, 36:20482–20494, 2023. 2

[23] Edward J Hu, Yelong Shen, Phillip Wallis, Zeyuan Allen-Zhu, Yuanzhi Li, Shean Wang, Lu Wang, and Weizhu Chen. Lora: Low-rank adaptation of large language models. *arXiv preprint arXiv:2106.09685*, 2021. 2

[24] Shengchao Hu, Li Chen, Penghao Wu, Hongyang Li, Junchi Yan, and Dacheng Tao. St-p3: End-to-end vision-based autonomous driving via spatial-temporal feature learning. In *European Conference on Computer Vision*, pages 533–549. Springer, 2022. 2

[25] Yihan Hu, Jiazhi Yang, Li Chen, Keyu Li, Chonghao Sima, Xizhou Zhu, Siqi Chai, Senyao Du, Tianwei Lin, Wenhai Wang, et al. Planning-oriented autonomous driving. In *Proceedings of the IEEE/CVF Conference on Computer Vision and Pattern Recognition*, pages 17853–17862, 2023. 1, 2, 6, 7

[26] Jyh-Jing Hwang, Runsheng Xu, Hubert Lin, Wei-Chih Hung, Jingwei Ji, Kristy Choi, Di Huang, Tong He, Paul Covington, Benjamin Sapp, Yin Zhou, James Guo, Dragomir Anguelov, and Mingxing Tan. Emma: End-to-end multimodal model for autonomous driving, 2024. 3

[27] Maximilian Igl, Daewoo Kim, Alex Kuefler, Paul Mougin, Punit Shah, Kyriacos Shiarlis, Dragomir Anguelov, Mark Palatucci, Brandyn White, and Shimon Whiteson. Symphony: Learning realistic and diverse agents for autonomous driving simulation. In *2022 International Conference on Robotics and Automation (ICRA)*, pages 2445–2451. IEEE, 2022. 3

[28] Bo Jiang, Shaoyu Chen, Qing Xu, Bencheng Liao, Jiajie Chen, Helong Zhou, Qian Zhang, Wenyu Liu, Chang Huang, and Xinggang Wang. Vad: Vectorized scene representation for efficient autonomous driving. In *Proceedings of the IEEE/CVF International Conference on Computer Vision*, pages 8340–8350, 2023. 1, 2, 6, 7

[29] Jinkyu Kim, Anna Rohrbach, Trevor Darrell, John Canny, and Zeynep Akata. Textual explanations for self-driving vehicles. In *Proceedings of the European conference on computer vision (ECCV)*, pages 563–578, 2018. 6

[30] Junnan Li, Dongxu Li, Silvio Savarese, and Steven Hoi. Blip-2: Bootstrapping language-image pre-training with frozen image encoders and large language models. In *International conference on machine learning*, pages 19730–19742. PMLR, 2023. 2

[31] Zhiqi Li, Wenhai Wang, Hongyang Li, Enze Xie, Chonghao Sima, Tong Lu, Yu Qiao, and Jifeng Dai. Bevformer: Learning bird’s-eye-view representation from multi-camera images via spatiotemporal transformers. In *European conference on computer vision*, pages 1–18. Springer, 2022. 2, 3, 5

[32] Zhiqi Li, Zhiding Yu, Shiyi Lan, Jiahua Li, Jan Kautz, Tong Lu, and Jose M Alvarez. Is ego status all you need for open-loop end-to-end autonomous driving? In *Proceedings of the IEEE/CVF Conference on Computer Vision and Pattern Recognition*, pages 14864–14873, 2024. 2, 3, 8

[33] Bencheng Liao, Shaoyu Chen, Xinggang Wang, Tianheng Cheng, Qian Zhang, Wenyu Liu, and Chang Huang. Maptr: Structured modeling and learning for online vectorized hd map construction. In *The Eleventh International Conference on Learning Representations*. 2

[34] Haotian Liu, Chunyuan Li, Qingyang Wu, and Yong Jae Lee. Visual instruction tuning. *Advances in neural information processing systems*, 36, 2024. 2

[35] Zhijian Liu, Haotian Tang, Alexander Amini, Xinyu Yang, Huizi Mao, Daniela L Rus, and Song Han. Bevfusion: Multi-task multi-sensor fusion with unified bird’s-eye view representation. In *2023 IEEE international conference on robotics and automation (ICRA)*, pages 2774–2781. IEEE, 2023. 2, 3

[36] Xianzheng Ma, Yash Bhalgat, Brandon Smart, Shuai Chen, Xinghui Li, Jian Ding, Jindong Gu, Dave Zhenyu Chen, Songyou Peng, Jia-Wang Bian, et al. When llms step into the 3d world: A survey and meta-analysis of 3d tasks via multi-modal large language models. *arXiv preprint arXiv:2405.10255*, 2024. 3

[37] Yingzi Ma, Yulong Cao, Jiachen Sun, Marco Pavone, and Chaowei Xiao. Dolphins: Multimodal language model for driving. *arXiv preprint arXiv:2312.00438*, 2023. 2

[38] Jiageng Mao, Yuxi Qian, Junjie Ye, Hang Zhao, and Yue Wang. Gpt-driver: Learning to drive with gpt. *arXiv preprint arXiv:2310.01415*, 2023. 2, 7

[39] Jiageng Mao, Junjie Ye, Yuxi Qian, Marco Pavone, and Yue Wang. A language agent for autonomous driving. *arXiv preprint arXiv:2311.10813*, 2023. 2

[40] Brandon McKinzie, Zhe Gan, Jean-Philippe Fauconnier, Sam Dodge, Bowen Zhang, Philipp Dufter, Dhruti Shah, Xianzhi Du, Futang Peng, Floris Weers, et al. Mml1: Methods, analysis & insights from multimodal llm pre-training. *arXiv preprint arXiv:2403.09611*, 2024. 2

[41] Nigamaa Nayakanti, Rami Al-Rfou, Aurick Zhou, Kratarth Goel, Khaled S Refaat, and Benjamin Sapp. Wayformer: Motion forecasting via simple & efficient attention networks. In *2023 IEEE International Conference on Robotics and Automation (ICRA)*, pages 2980–2987. IEEE, 2023. 2

[42] OpenAI. Gpt-4v(ision) system card, 2023. 1, 2

[43] Dean A Pomerleau. Alvinn: An autonomous land vehicle in a neural network. *Advances in neural information processing systems*, 1, 1988. 1

[44] C. Qi, Yin Zhou, Mahyar Najibi, Pei Sun, Khoa T. Vo, Boyang Deng, and Dragomir Anguelov. Offboard 3d object detection from point cloud sequences. *2021 IEEE/CVF Conference on Computer Vision and Pattern Recognition (CVPR)*, pages 6130–6140, 2021. 7

[45] Alec Radford, Jong Wook Kim, Chris Hallacy, Aditya Ramesh, Gabriel Goh, Sandhini Agarwal, Girish Sastry, Amanda Askell, Pamela Mishkin, Jack Clark, et al. Learning transferable visual models from natural language supervision. In *International conference on machine learning*, pages 8748–8763. PMLR, 2021. 2

[46] Ari Seff, Brian Cera, Dian Chen, Mason Ng, Aurick Zhou, Nigamaa Nayakanti, Khaled S Refaat, Rami Al-Rfou, and Benjamin Sapp. Motionlm: Multi-agent motion forecasting as language modeling. In *Proceedings of the IEEE/CVF*

*International Conference on Computer Vision*, pages 8579–8590, 2023. [2](#), [7](#), [4](#)

[47] Hao Sha, Yao Mu, Yuxuan Jiang, Li Chen, Chenfeng Xu, Ping Luo, Shengbo Eben Li, Masayoshi Tomizuka, Wei Zhan, and Mingyu Ding. Languagempc: Large language models as decision makers for autonomous driving. *arXiv preprint arXiv:2310.03026*, 2023. [2](#)

[48] Hao Shao, Yuxuan Hu, Letian Wang, Guanglu Song, Steven L Waslander, Yu Liu, and Hongsheng Li. Lmdrive: Closed-loop end-to-end driving with large language models. In *Proceedings of the IEEE/CVF Conference on Computer Vision and Pattern Recognition*, pages 15120–15130, 2024. [2](#)

[49] Chonghao Sima, Katrin Renz, Kashyap Chitta, Li Chen, Hanxue Zhang, Chengan Xie, Jens Beißenwenger, Ping Luo, Andreas Geiger, and Hongyang Li. Drivelm: Driving with graph visual question answering. In *First Vision and Language for Autonomous Driving and Robotics Workshop*. [2](#), [6](#), [8](#), [4](#)

[50] Yi Tay, Mostafa Dehghani, Vinh Q Tran, Xavier Garcia, Jason Wei, Xuezhi Wang, Hyung Won Chung, Siamak Shakeri, Dara Bahri, Tal Schuster, et al. UI2: Unifying language learning paradigms. *arXiv preprint arXiv:2205.05131*, 2022. [6](#)

[51] Gemini Team, Rohan Anil, Sebastian Borgeaud, Jean-Baptiste Alayrac, Jiahui Yu, Radu Soricut, Johan Schalkwyk, Andrew M Dai, Anja Hauth, Katie Millican, et al. Gemini: a family of highly capable multimodal models. *arXiv preprint arXiv:2312.11805*, 2023. [1](#), [2](#), [3](#)

[52] Thomas Tian, Boyi Li, Xinshuo Weng, Yuxiao Chen, Edward Schmerling, Yue Wang, Boris Ivanovic, and Marco Pavone. Tokenize the world into object-level knowledge to address long-tail events in autonomous driving. In *Workshop on Language and Robot Learning: Language as an Interface*. [2](#)

[53] Xiaoyu Tian, Junru Gu, Bailin Li, Yicheng Liu, Chenxu Hu, Yang Wang, Kun Zhan, Peng Jia, Xianpeng Lang, and Hang Zhao. Drivevlm: The convergence of autonomous driving and large vision-language models. *arXiv preprint arXiv:2402.12289*, 2024. [1](#), [2](#), [3](#), [6](#), [7](#)

[54] Balakrishnan Varadarajan, Ahmed Hefny, Avikalp Srivastava, Khaled S Refaat, Nigamaa Nayakanti, Andre Cornman, Kan Chen, Bertrand Douillard, Chi Pang Lam, Dragomir Anguelov, et al. Multipath++: Efficient information fusion and trajectory aggregation for behavior prediction. In *2022 International Conference on Robotics and Automation (ICRA)*, pages 7814–7821. IEEE, 2022. [2](#)

[55] Shihao Wang, Zhiding Yu, Xiaohui Jiang, Shiyi Lan, Min Shi, Nadine Chang, Jan Kautz, Ying Li, and Jose M Alvarez. Omnidrive: A holistic llm-agent framework for autonomous driving with 3d perception, reasoning and planning. *arXiv preprint arXiv:2405.01533*, 2024. [7](#), [8](#)

[56] Jason Wei, Xuezhi Wang, Dale Schuurmans, Maarten Bosma, Fei Xia, Ed Chi, Quoc V Le, Denny Zhou, et al. Chain-of-thought prompting elicits reasoning in large language models. *Advances in neural information processing systems*, 35:24824–24837, 2022. [2](#), [3](#)

[57] Xinshuo Weng, Boris Ivanovic, Yan Wang, Yue Wang, and Marco Pavone. Para-drive: Parallelized architecture for real-time autonomous driving. In *Proceedings of the IEEE/CVF Conference on Computer Vision and Pattern Recognition*, pages 15449–15458, 2024. [1](#), [7](#)

[58] Penghao Wu, Xiaosong Jia, Li Chen, Junchi Yan, Hongyang Li, and Yu Qiao. Trajectory-guided control prediction for end-to-end autonomous driving: A simple yet strong baseline. *Advances in Neural Information Processing Systems*, 35:6119–6132, 2022. [2](#)

[59] xAI. Grok-1.5 vision preview, 2024. [2](#)

[60] Yichen Xie, Chenfeng Xu, Marie-Julie Rakotosaona, Patrick Rim, Federico Tombari, Kurt Keutzer, Masayoshi Tomizuka, and Wei Zhan. Sparsefusion: Fusing multi-modal sparse representations for multi-sensor 3d object detection. In *Proceedings of the IEEE/CVF International Conference on Computer Vision*, pages 17591–17602, 2023. [2](#)

[61] Zhenhua Xu, Yujia Zhang, Enze Xie, Zhen Zhao, Yong Guo, Kwan-Yee K Wong, Zhenguo Li, and Hengshuang Zhao. Drivegpt4: Interpretable end-to-end autonomous driving via large language model. *IEEE Robotics and Automation Letters*, 2024. [1](#), [2](#), [6](#)

[62] Jiang-Tian Zhai, Ze Feng, Jihao Du, Yongqiang Mao, Jiang-Jiang Liu, Zichang Tan, Yifu Zhang, Xiaoqing Ye, and Jing-dong Wang. Rethinking the open-loop evaluation of end-to-end autonomous driving in nuscenes. *arXiv preprint arXiv:2305.10430*, 2023. [3](#), [8](#)

[63] Xiaohua Zhai, Basil Mustafa, Alexander Kolesnikov, and Lucas Beyer. Sigmoid loss for language image pre-training. In *Proceedings of the IEEE/CVF International Conference on Computer Vision*, pages 11975–11986, 2023. [2](#)

[64] Lianmin Zheng, Wei-Lin Chiang, Ying Sheng, Siyuan Zhuang, Zhanghao Wu, Yonghao Zhuang, Zi Lin, Zhuohan Li, Dacheng Li, Eric. P Xing, Hao Zhang, Joseph E. Gonzalez, and Ion Stoica. Judging llm-as-a-judge with mt-bench and chatbot arena, 2023. [2](#)

[65] Wenzhao Zheng, Weiliang Chen, Yuanhui Huang, Borui Zhang, Yueqi Duan, and Jiwen Lu. Occworld: Learning a 3d occupancy world model for autonomous driving. *arXiv preprint arXiv:2311.16038*, 2023. [2](#)

[66] Wenzhao Zheng, Ruiqi Song, Xianda Guo, and Long Chen. Genad: Generative end-to-end autonomous driving. *arXiv preprint arXiv:2402.11502*, 2024. [2](#)

# S4-Driver: Scalable Self-Supervised Driving Multimodal Large Language Model with Spatio-Temporal Visual Representation

## Supplementary Material

The supplementary material is organized as follows. Sec. 7 provides implementation details of our proposed methods including the concrete input prompt and target output. Sec. 8 provides the model performance for each ego-vehicle behavior separately. Sec. 9 gives additional visualization of S4-Driver motion planning in diverse scenarios. Finally, Sec. 10 conducts extra ablation studies on WOMD-Planning-ADE benchmark to justify the design of S4-Driver.

### 7. Implementation Details

**WOMD-Planning-ADE benchmark.** This benchmark contains 487k scenarios for model training and 44k for validation, which are divided from 103k sequences of 20s length. Each scenario contains 1s history and 8s future. We only consider the future 5s for the open-loop evaluation of motion planning since motion planning in real task is conducted in an iterative manner. At each time stamp, the dataset provides multi-view images captured by 8 cameras (namely *front left*, *front*, *front right*, *side left*, *side right*, *rear left*, *rear*, *rear right*). The dataset is also equipped with fine-grained labels for all the other agents and the roadgraph although they are not used in our self-supervised motion planning algorithm.

**Ego-vehicle coordinate system.** We conduct the motion planning task in the ego-vehicle coordinate system. At current timestamp, the ego-vehicle position is defined as the origin. The  $x$ -axis is oriented towards the current heading angle of the ego-vehicle. The  $y$ -axis is oriented towards the left of the ego-vehicle. The  $z$ -axis is oriented upwards. Although it is a 3D coordinate system, we only consider the  $xy$ -plane for the description of the positions, velocities, and accelerations of the vehicles in the motion planning task.

**Architecture and hyperparameters.** Unless otherwise specified, we build up the S4-Driver framework based on multimodal large-language model PaLI3-5B [10]. The 3D scene representation (Sec. 3.3) in default covers the range of  $(-30m, 80m) \times (-30m, 30m) \times (-2m, 8m)$  in the ego-vehicle coordinate along  $x, y, z$  axes separately. The position embedding in Eq. 3 and Eq. 7 are implemented with a two-layer MLP attached to the Fourier embedding of  $(x, y, z)$ . To generate the gate values, we reduce the dimension of visual features from  $C = 1536$  to  $C' = 96$

in Eq. 5. The volume resolution is  $1m \times 1m \times 2m$ . For each scene, we select  $M = 6000$  sparse volumes based on the gate values. For attention bias (Sec. 3.3.3), there are independent intra-modality biases for visual tokens and text tokens separately. We leave the details of bias function  $b(\cdot)$  in the extra ablation study (Sec. 10). For each attention head at each self-attention layer, we also include learnable scalar inter-modality biases for the attention values between text tokens and visual tokens. In Sec. 3.4, for temporal fusion, apart from the current frame, we also take camera images from  $T = 1$  historical frame at the timestamp  $-0.5s$  as model input. For multi-decoding aggregation (Sec. 3.5), the model outputs  $K = 16$  trajectories in parallel through Top- $p$  sampling (nucleus sampling) [21] ( $p = 0.9$ ), which are aggregated as one unique planning result. For both datasets, the input images are resized to  $448 \times 448$  as model inputs.

**Model initialization.** To ensure the alignment within the pretrained MLLM, we apply the following special rules to relieve the disturbance of injected modules to the pretrained weights in the early finetuning stage. The last FC-layer of MLP for the position embeddings in Eq. 3 and Eq. 7 are zero initialized. The learnable vacant feature  $\mathbf{f}_{vac}$  for sparse volume representation is also initialized as zeros (Eq. 8). We also set the initial bias for each bin in the bias function  $b(\cdot)$  (Eq. 9) as zeros (details in Sec. 10). Finally, the temporal fusion (Sec. 3.4), we maintain the channel-wise semantics of visual features by initializing the weight matrix of the FC layer as  $\mathbf{W} = [I \in \mathbb{R}^{C \times C}; \mathbf{0}^{C \times (T-1) \cdot C}]$  and the bias as zero. Based on the above rules, the inserted modules would not significantly change the channel-wise semantics of the visual features from original pretrained perspective view features, which allows for a stable and efficient finetuning process.

**Input prompt and target output.** The input prompt is composed of the high-level behavior command and ego-vehicle historical states. We represent all historical states in the language space. The position, velocity, and acceleration at each time stamp are represented with two floating numbers (two decimal places) separately for the  $x$ -component and  $y$ -component in the ego-vehicle coordinate. The target output is composed of meta-decision (Sec. 3.2 only in S4-Driver) and future waypoints. The future waypoints are also represented in the language space with two floating numbers for each time stamp. The historical and future states are sampled at a frequency of 5Hz on WOMD-Planning-ADE

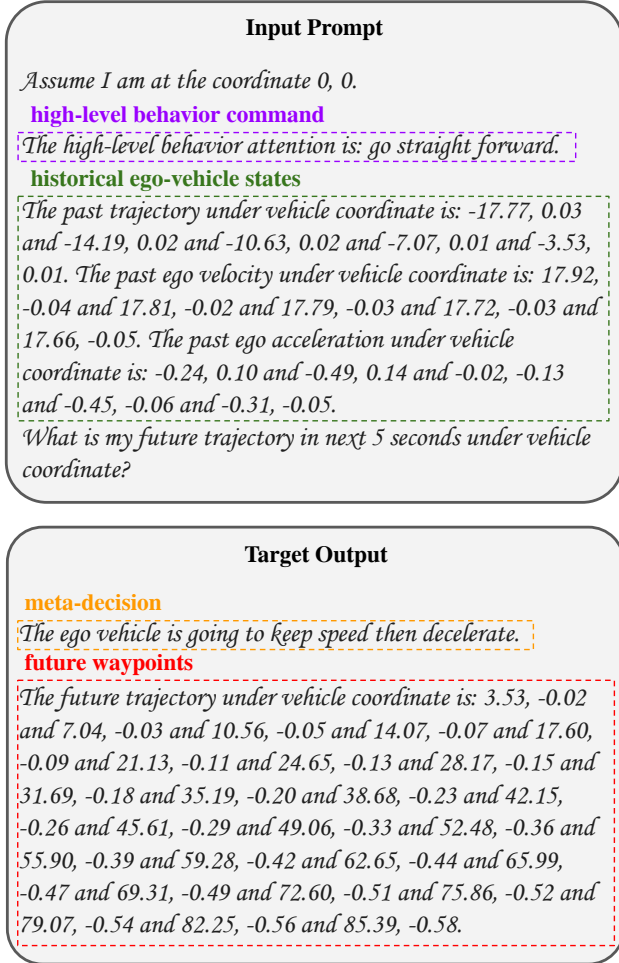


Figure 9. Example input prompt and target output on WOMD-Planning-ADE.

where we consider the historical states of past 1s and future waypoints of future 5s. On nuScenes dataset, we consider the historical states of past 1s and future waypoints of future 3s at a frequency of 2Hz. An example of the input and output on WOMD-Planning-ADE is visualized in Fig. 9.

**Heuristics for high-level behaviors.** We consider the seven behaviors for the ego-vehicle on WOMD-Planning-ADE benchmark, which are determined based on the ego-vehicle ground-truth future trajectories following heuristic rules.

1. **Stop:** The ego-vehicle movement is  $< 5m$  and the maximal speed is  $< 2m/s$ .
2. **Do left turn:** The ego-vehicle does not stop. The final heading angle is  $> 30^\circ$ . The final position is  $\geq -5m$  along  $x$ -axis.
3. **Do left U-turn:** The ego-vehicle does not stop. The final heading angle is  $> 30^\circ$ . The final displacement is  $< -5m$  along  $x$ -axis.

4. **Do right turn:** The ego-vehicle does not stop. The final heading angle is  $< -30^\circ$ .
5. **Go straight left:** The ego-vehicle does not stop. The final heading angle is in the range  $[-30^\circ, 30^\circ]$ . The final displacement is  $> 5m$  along  $y$ -axis.
6. **Go straight right:** The ego-vehicle does not stop. The final heading angle is in the range  $[-30^\circ, 30^\circ]$ . The final displacement is  $< -5m$  along  $y$ -axis.
7. **Go straight forward:** The ego-vehicle does not stop. The final heading angle is in the range  $[-30^\circ, 30^\circ]$ . The final displacement along  $y$ -axis is in the range  $[-5m, 5m]$ .

For the calculation of *bADE* metric in the model evaluation, we follow the above rules to determine the behavior based on the ground-truth future trajectories of 8s although our planning horizon is only 5s. For the high-level behavior command in the model inputs, “stop” is excluded to avoid future information leakage. To determine the high-level behavior command input, we start from the ground-truth 8s future trajectories. If none of behaviors 2-7 is satisfied, we would prolong the future horizon by 2s until at least one of behaviors 2-7 is satisfied. If the end of the collected trajectory sequence is reached, we would just consider that scenario as “go straight forward”.

**Heuristics for meta-decisions.** In Sec. 3.2, we design a meta-decision strategy as a preliminary prediction before the waypoints. The meta-decision of ego-vehicle includes four categories determined with following heuristic rules based on the ground-truth future information.

1. **Keep stationary:** The maximal speed is  $< 2m/s$  and the final displacement is  $< 1.5m$ .
2. **Keep speed:** The ego-vehicle does not keep stationary. The average acceleration is in the range of  $[-0.5m/s^2, 0.5m/s^2]$ .
3. **Accelerate:** The ego-vehicle does not keep stationary. The average acceleration is  $> 0.5m/s^2$ .
4. **Decelerate:** The ego-vehicle does not keep stationary. The average acceleration is  $< -0.5m/s^2$ .

The model should firstly predict the meta-decision and then auto-regressively output the future waypoints. On WOMD-Planning-ADE with 5s future prediction horizon, we divide the 5s into two stages of 2.5s, where meta-decisions are predicted independently for each stage. On nuScenes dataset with 3s prediction horizon, we only consider one-stage meta-decision.

## 8. Behavior-wise Model Performance

In Tab. 7, we report the *ADE@5s* metric of S4-Driver for each ego-vehicle behavior on WOMD-Planning-ADE benchmark separately. Results show the superiority of S4-Driver especially in complicated scenarios like turnings,

Methods	ADE@5s for each behavior								ADE@5s	bADE@5s
	stop	straight forward	straight left	straight right	left turn	right turn	left U-turn			
Vanilla PaLI	<b>0.048</b>	0.960	1.252	1.297	1.566	1.323	1.039	0.798	1.069	
S4-Driver (ours)	0.063	0.843	1.077	1.177	1.252	1.158	0.925	0.693	0.928	
S4-Driver* (ours)	0.065	<b>0.806</b>	<b>0.957</b>	<b>1.074</b>	<b>1.124</b>	<b>1.027</b>	<b>0.756</b>	<b>0.655</b>	<b>0.830</b>	
<i>Models that take high-quality objects, tracks, and roadgraphs as inputs instead of using raw camera images.</i>										
MotionLM	0.048	0.832	1.293	1.275	1.239	1.172	0.990	0.697	0.978	

Table 7. Behavior-wise sliced metrics on WOMD-Planning-ADE benchmark. “\*” denotes methods with internal data pretraining.

Camera configuration	ADE@5s	bADE@5s
<i>front</i>	0.765	1.036
<i>front, front left/right</i>	0.751	1.012
<i>front, front left/right, side left/right</i>	0.746	<b>0.981</b>
<i>all eight surrounding cameras</i>	<b>0.732</b>	0.985

Table 8. Ablation studies on camera configurations.

where a significant performance gain is witnessed from vanilla PaLI baseline to S4-Driver. Motion planning for these difficult behaviors requires a great understanding of the roadgraph and other agents from raw camera images, which reflects the strong reasoning ability of our proposed spatio-temporal visual representation.

## 9. Additional Qualitative Results

In Fig. 10, we visualize more planning results on WOMD-Planning-ADE. Examples cover different behaviors, speeds, lighting conditions, and weathers. Results show the robust performance of S4-Driver in all these diverse scenarios.

## 10. Additional Ablation Studies

In this part, we conduct several additional ablation studies to further justify the design of our S4-Driver including the camera configuration, relative attention bias, multi-decoding aggregation, and motion tokens.

**Camera configuration.** We apply different configurations of camera sensors in Tab. 8. Consistent with intuitions, the *front* camera is the most important, which can solely guarantee a reasonable planning performance. Adding other cameras continuously improves the model performance since they provide more and more complete information of the surrounding environment. The three cameras in the back can notably boost the planning model since they provide cues about other agents behind ego-vehicle. This information helps to determine the future ego-vehicle velocities and accelerations.

**Relative attention bias.** We consider two types of relative position bias function  $b(\cdot)$  in Eq. 9.

**1. Linear bias:** The bias is linearly related to the relative distance between tokens. For the sparse volume visual tokens,  $b(x, y, z) = b_x(\Delta x) + b_y(\Delta y) + b_z(\Delta z)$ , we take the  $x$ -axis as an example,

$$b_x(\Delta x) = \tau_x \cdot |\Delta x|, \quad (14)$$

where  $\tau_x$  is a learnable parameter separately for each attention head at each layer, and  $\Delta x$  is the relative position between sparse volume tokens along  $x$ -axis. Similarly, for 1D text tokens, the separate bias function is

$$b_p(\Delta p) = \tau_p \cdot |\Delta p| \quad (15)$$

where  $\tau_p$  is a learnable parameter separately for each attention head in each layer, and  $\Delta p$  is the relative position between text tokens.

**2. Bin-wise bias (our choice):** The relative positions  $\Delta x, \Delta y, \Delta z$  (visual tokens) and  $\Delta p$  (text tokens) for each axis are divided into 32 bins independently. For each axis, 16 bins cover the range  $[-8(m), 8(m)]$  linearly with an interval  $1(m)$ <sup>2</sup>. The other 16 bins symmetrically cover the range  $(-128(m), -8(m))$  and  $(8(m), 128(m))$  in log scale, where the relative distances are truncated to at most  $128(m)$ . In this case, if we take  $b_x(\cdot)$  as an example, the relative bias function is written as

$$b_x(\Delta x) = m_x(\text{bin}(\Delta x)) \quad (16)$$

where  $m_x(\cdot)$  maps each bin to a learnable bias value independently for each attention head at each self-attention layer.

Tab. 9 justifies the design of bin-wise bias, which brings greatly better performance. We think it is important to distinguish the two directions along each axis (*e.g.* front or back) in the motion planning task. Besides, local feature aggregation is more sensitive to close neighbors at each locality, so the bin-wise bias function has finer grains in close distance compared to the linear bias function.

**Multi-decoding aggregation.** We dig into the multi-decoding strategy which can bring notable performance

<sup>2</sup>The unit (m) is only for visual tokens ( $\Delta x, \Delta y, \Delta z$ ) throughout this paragraph.



Figure 10. Additional qualitative results of motion planning. We show the *front left*, *front*, *front right* cameras for each case.

Attention bias	ADE@5s	bADE@5s
no bias	0.750	1.005
linear bias function	0.770	1.082
bin-wise bias function	<b>0.732</b>	<b>0.985</b>

Table 9. Ablation studies on attention bias.

gain. The motivation is that the MLLM is prone to assigning high confidence scores to simple future behaviors such as *stop*. To this end, we encourage the model to output multiple future trajectories. Their aggregation serves as the final planning result, which can counteract the model’s high confidence in simple behaviors. In Tab. 10, we find that 1) The aggregation of more decoded trajectories leads to better performance. 2) Nucleus sampling can outperform beam search since it can generate more diverse outputs. 3) Weighted average is inferior to mean average since the model is prone to assigning high confidence to simple degenerated behaviors.

**Motion tokens.** Several prior works [46, 49] benefit from specialized trajectory tokenization modules, which converts motion trajectories into extra discrete tokens added to the vocabulary of language models. However, in

Sample number	Sample strategy	Aggregation	ADE@5s	bADE@5s
1	greedy sampling	-	0.728	0.986
4	beam search	average	0.739	0.997
4	nucleus sampling	average	0.709	0.941
4	nucleus sampling	weighted average	0.747	1.005
16	nucleus sampling	average	<b>0.693</b>	<b>0.928</b>

Table 10. Ablation studies on multi-decoding aggregation.

Trajectory representation	ADE@5s	bADE@5s
motion tokens	0.779	1.061
floating numbers	<b>0.750</b>	<b>1.005</b>

Table 11. Ablation studies on motion trajectory tokenization.

Tab. 11, the trajectory tokenization strategy similar with MotionLM [46] hurts the performance of our S4-Driver in comparison with naïve floating number waypoints representation (Fig. 9). We also witness a much slower convergence speed with this extra trajectory tokenization. Since the MLLM is already pretrained on large-scale data, additionally injected trajectory tokens may not align with the pretrained model. In contrast, the floating number representation can align the historical and future states in the language space to exploit the large-scale MLLM pretraining with lower requirement for finetuning.